The inverse source problem based on the radiative transfer equation in optical molecular imaging

Alexander D. Klose [a,*], Vasilis Ntziachristos [b], Andreas H. Hielscher [a]

[a] *Departments of Biomedical Engineering and Radiology, Columbia University, ET351 Mudd Building, MC 8904, 500 West 120th Street, New York, NY 10027, USA*
[b] *Center for Molecular Imaging Research, Massachusetts General Hospital & Harvard Medical School, Charlestown, MA 02129, USA*

Abstract

We present the first tomographic reconstruction algorithm for optical molecular imaging that is based on the equation of radiative transfer. The reconstruction code recovers the spatial distribution of fluorescent sources in highly scattering biological tissue. An objective function, which describes the discrepancy of measured near-infrared light with predicted numerical data on the tissue surface, is iteratively minimized to find a solution of the inverse source problem. At each iteration step the predicted data are calculated by a forward model for light propagation based on the equation of radiative transfer. The unknown source distribution is updated along a search direction that is provided by an adjoint differentiation technique.
© 2004 Elsevier Inc. All rights reserved.

1. Introduction

Traditional biomedical imaging techniques differentiate pathological from normal tissue by detecting macroscopic changes in tissue structures. Using molecular imaging, on the other hand, one tries to monitor the development of disease-associated processes on a molecular level prior to the appearance of macroscopic tissue changes. Specifically designed molecular probes are used as source of image contrast. Tomographic imaging techniques, such as positron emission tomography (PET), single photon emission

---

[*] Corresponding author. Tel.: +1 212 854 5868; fax: +1 212 854 8725.
E-mail address: ak2083@columbia.edu (A.D. Klose).

computed tomography (SPECT), and magnetic resonance tomography (MRI), have already widely adopted the concept of this new imaging modality, and have been successful in imaging of gene expressions, protein–protein interactions, and drug effects at a cellular and molecular level [1–8]. In addition optical molecular imaging has emerged which uses near-infrared fluorescent probes [1,9–14]. A fluorescent biochemical marker is injected into a biological system and will emit near-infrared light upon excitation by an external light source. From measurements of the light intensity on the tissue surface one seeks to determine the spatial concentration distribution of the marker inside the tissue. Different biochemical mechanisms within the tissue can influence the fluorescent probe concentration distribution. For example, the biochemical marker accumulates in tissue parts with specific targets such as cell receptors [10,11,15–17], or the fluorophore is quenched in its native state and only emits light after activation, i.e. when a specific enzyme is encountered [10,11,18–20]. In both cases the fluorescent light signal is proportional to the accumulated or activated fluorescent probe concentration. Most work in optical molecular imaging has been limited to direct imaging of fluorescent light that escapes the surface of small animals [10,12,15,18,21,22]. In this instance, an exact localization of light-emitting sources inside the tissue is not possible. However, fluorescent source distributions in small animals could be determined by recording tomographical data sets and employing appropriate tomographic image reconstruction schemes [19,20,23].

A major difficulty in determining the fluorescent source distribution is imposed by multiple scattering of photons that propagate through biological tissue. The mean free path of scattered photons in biological tissue is typically in the range 10^{-1}–10^{-3} cm for near-infrared light. That limits the application of well-established image reconstruction methods of transmission and emission tomography. For example, X-ray computed tomography (CT) deals only with non-scattered or single-scattered photons and the particle transport within the tissue can be described by a solution of an integral equation [24]. An inversion formula is used to determine the tissue parameters of interest such as the X-ray attenuation coefficient. In emission tomography, such as PET or SPECT, similar inversion formulas can be employed.

In contrast to CT which requires the solution of an integral equation, in near-infrared fluorescence tomography an integro-differential equation needs to be solved that takes multiple scattering into account. This integro-differential equation is known as equation of radiative transfer (ERT). Solving the ERT for a given fluorescent source distribution is also referred to as solving the forward problem. The problem of finding the fluorescence source distribution from measured light intensities on the tissue surface is called the inverse problem.

To solve the inverse source problem in highly scattering media using the ERT one can use explicit and implicit methods [25]. Explicit methods provide analytical solutions to the inverse source problem directly from measured data. No forward problem for radiative transfer needs to be solved. Explicit methods based on the ERT are limited to simple medium geometries with spatially non-varying optical parameters [26–30]. For more complex geometries and heterogeneous media no explicit methods are available and implicit methods need to be employed.

Implicit methods for solving the inverse source problem iteratively utilize a solution of a forward model to provide predicted measurement data. An update of an initial source distribution is sought by minimizing a functional that describes the goodness of a fit between the predicted and experimental data. Implicit methods are computationally expensive when the forward model is based on the ERT. Implicit methods based on the ERT have been used before in various scientific fields such as in inverse heat source problems or inverse hydrologic bioluminescence problems [25,31–36], but not yet in optical molecular imaging.

The inverse fluorescent source problem in optical molecular imaging has already been solved using the diffusion equation as a forward model for light propagation [37–48]. The diffusion model is an approximation to the ERT and has limitations in optically thin media, in media with small geometries where boundary effects are dominant, and in media where sources and detectors are not sufficiently far apart [49–52]. This poses particular problems, for example, in the area of small animal fluorescence imaging, where fluorescent sources are potentially very close to detectors on the tissue surface.

An image reconstruction method based on the ERT has the potential to overcome these limitations. Therefore, we have developed a tomographic reconstruction scheme based on the ERT that solves the inverse fluorescent source problem by recovering the spatial distribution of fluorescent sources in scattering media. This method is similar to a previously developed reconstruction scheme that was applied to a different inverse problem in optical tomography, where the unknown spatial distribution of the intrinsic absorption and scattering properties of biological tissue was sought [53–56].

Our fluorescence image reconstruction technique is an implicit method and can be viewed as a nonlinear optimization approach. A forward model for light transport based on the ERT predicts the detector readings on the tissue boundary for a given initial source distribution. An objective function is defined that is the χ^2-error norm of the predicted and measured detector readings. An updating scheme is used to iteratively modify the initial distribution along a search direction and determines a new source distribution inside the medium. The search direction is provided by the derivative of the objective function with respect to the present source distribution. The optimization process is finished after the measured and predicted data match and a minimum of the objective function is found. The final source distribution is displayed in an image.

Besides using the ERT for the first time in optical molecular image reconstruction we also introduce an adjoint differentiation method as a novelty to fluorescence tomography. An adjoint differentiation technique computes the gradient of the objective function by exploiting the numerical structure of the light propagation model. The concept of the adjoint differentiation technique can also be applied to similar inverse problems or sensitivity analysis where the derivative of an error function is sought. A distinct advantage of using that technique is its relatively simple numerical implementation and the resulting low computational costs.

In a previous Letter we already presented first numerical results for reconstructing the absorption coefficient and the quantum yield of a two-dimensional fluorophore distribution using synthetic measurement data [57]. The image reconstruction method could be employed in two different modes, the absorption-contrast mode and fluorescent-contrast mode. The present article describes the physical and numerical details of the absorption contrast mode for reconstructing the fluorophore absorption coefficient. In addition to the previous work, we included partly reflected boundary conditions (Fresnel reflection) that take the refractive index mismatch at the air–tissue interface into account. Furthermore, for the first time we tested the reconstruction algorithm with experimental data obtained from a three-dimensional, anisotropically scattering, tissue-like fluorescent phantom.

In the following sections we will first describe the ERT-based forward model for light propagation in tissue using a finite-difference discrete-ordinates method. Next we present the nonlinear optimization technique that is used to minimize the objective function. This part includes specifics of the derivative calculation of the objective function by means of an adjoint differentiation technique. Finally, we illustrate the performance of the reconstruction code using experimental data.

2. Forward model for light propagation in tissue

The forward model of a fluorescent system in tissue consists of two stages: (1) excitation of fluorophores inside tissue and (2) subsequent emission of fluorescent light. External light sources with wavelength λ^x illuminate the tissue surface and the light propagates through the tissue. Fluorescent molecules in their ground state with a specific extinction coefficient ϵ in units of $M^{-1} cm^{-1}$ absorb the light and are elevated into an excited state. Some proportion, defined by the quantum yield η, of the excited fluorescent molecules emits again light at a different wavelength, $\lambda^m > \lambda^x$, and returns to its ground state. The fluorophore with concentration c in units of M constitutes an internal light source with the strength proportional to η and the fluorophore absorption $\mu_a^{x \to m} = c\epsilon$ in units of cm^{-1} at the excitation wavelength λ^x. The light originating from the fluorescent source distribution escapes the tissue and is measured at the tissue surface.

2.1. Equation of radiative transfer

The forward model for light propagation determines the fluorescent light distribution given an external excitation light source at the tissue boundary and a spatial distribution of optical properties. The light distribution for both the excitation and emission wavelengths can be described by a hierarchal system of two time-independent ERTs for the radiance $\psi(r, \Omega)$ with units of W cm^{-2} sr^{-1}. The first equation of radiative transfer (ERT I) describes the propagation of the excitation light at the wavelength λ^x originating from an external light source $S^x(r, \Omega)$ with units of W cm^{-3} sr^{-1}. The ERT is an energy balance equation for the radiance $\psi^x(r, \Omega)$ and is given as

$$\Omega \cdot \nabla \psi^x + (\mu_a^{x\rightarrow} + \mu_a^{x\rightarrow m} + \mu_s^x)\psi^x = \mu_s^x \int_{4\pi} p(\Omega \cdot \Omega')\psi^x(\Omega')d\Omega' + S^x. \tag{1}$$

Here, the spatial position $r = (x, y, z)$ of the radiance is given in Cartesian coordinates. The direction $\Omega = (\vartheta, \varphi)$ of the radiance is given in spherical coordinates, but can also be expressed in Cartesian coordinates $\Omega = (\xi, \eta, \mu)$ with

$$\xi = \sin\vartheta\cos\varphi,$$
$$\eta = \sin\vartheta\sin\varphi, \tag{2}$$
$$\mu = \cos\vartheta.$$

Both coordinate systems are shown in Fig. 1. The propagating light undergoes scattering and absorption processes that are described by the scattering, $\mu_s^x(r)$, and absorption, $\mu_a^x(r)$, coefficients at the wavelength λ^x in units of cm^{-1}. The absorption coefficient $\mu_a^x(r)$ consists of the intrinsic absorption $\mu_a^{x\rightarrow}(r)$ of the tissue and the absorption $\mu_a^{x\rightarrow m}(r)$ due to the fluorochrome. The scattering phase function $p(\Omega \cdot \Omega')$ with units of sr^{-1} gives the probability that a single photon coming from Ω' is deflected by an angle θ into Ω. The angle θ encloses the directions formed by Ω and Ω' in the interval $\theta \in [0, \pi]$ with $\Omega \cdot \Omega' = \cos\theta$. A commonly applied scattering phase function in tissue optics is the Henyey–Greenstein function [58–60], which is given by

$$p(\cos\theta) = \frac{1 - g^2}{4\pi(1 + g^2 - 2g\cos\theta)^{3/2}} \tag{3}$$

with the normalization condition
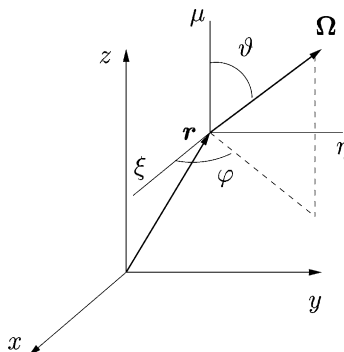
$$2\pi \int_{-1}^{1} p(\cos\theta)d\cos\theta = 1. \tag{4}$$

Fig. 1. Coordinate systems for spatial position r and direction Ω.

The radiation field described by the ERT I [Eq. (1)] excites fluorescent molecules at position r. The amount of excited fluorescent molecules depends linearly on the absorbed fluence $\phi^x(r)$ if saturation and bleaching effects are neglected. The fluence distribution $\phi^x(r)$ in units of W cm^{-2} is obtained by integrating the radiance $\psi^x(r, \Omega)$ at position r over all directions Ω:

$$\phi^x(r) = \int_{4\pi} \psi^x(r, \Omega) d\Omega. \tag{5}$$

The excited fluorophore with the quantum yield η and absorption coefficient $\mu_a^{x \to m}(r)$ constitutes a light source at the fluorescence wavelength λ^m with the strength

$$S^m(r, \Omega) = \frac{1}{4\pi} \eta \mu_a^{x \to m}(r) \phi^x(r) \tag{6}$$

in units of W cm^{-3} sr^{-1}. It emits isotropic light since all directional information is lost after excitation.

The second equation of radiative transfer (ERT II) describes the light propagation at the wavelength λ^m originating from spatially distributed fluorescent light sources $S^m(r, \Omega)$. We obtain the ERT II with the fluorescent source term (6)

$$\Omega \cdot \nabla \psi^m + (\mu_a^m + \mu_s^m)\psi^m = \mu_s^m \int_{4\pi} p(\Omega \cdot \Omega')\psi^m(\Omega') d\Omega' + \frac{1}{4\pi} \eta \mu_a^{x \to m} \phi^x. \tag{7}$$

The radiance distribution $\psi^m(r, \Omega)$ depends on the optical tissue parameters, $\mu_a^m(r)$ and $\mu_s^m(r)$, at wavelength λ^m and on the fluorescent source distribution. The fluorescent light escapes through the tissue boundaries and is measured by a detector at position r_d. The light intensity $\phi^m(r_d)$ is given in units of W cm^{-2} with

$$\phi^m(r_d) = \int_{n \cdot \Omega > 0} \psi^m(r_d, \Omega) d\Omega \tag{8}$$

with n as the normal outward vector at the boundary.

2.2. Boundary condition

Biological tissue has an optical refractive index ($n > 1$) that is different from the refractive index of the surrounding medium such as air ($n_0 = 1$). Light is reflected and refracted when escaping the medium due to the refractive index mismatch ($n > n_0$) at the tissue–air interface. The escaping radiance $\psi(\Omega)$ along the outward direction Ω with $n \cdot \Omega > 0$ is partly reflected at the interface and contributes to the light propagation inside the tissue. Furthermore, some fraction of the light leaving the tissue along Ω changes its direction into Ω'' due to refraction. The relation between the outward direction Ω, the outward direction Ω'' of the refracted radiance, and the inward direction Ω' of the reflected radiance is shown in Fig. 2.

The radiance that is reflected back into the medium can be obtained from the relation

$$\psi(\Omega') = R\psi(\Omega), \quad n \cdot \Omega' < 0, \tag{9}$$

where R is the reflectivity, which determines the amount of reflected light. R is given by *Fresnel's law* [61]

$$R = \frac{1}{2} \left(\frac{\sin^2(\beta - \alpha)}{\sin^2(\beta + \alpha)} + \frac{\tan^2(\beta - \alpha)}{\tan^2(\beta + \alpha)} \right). \tag{10}$$

The angle α is enclosed by the normal vector n and the outward direction Ω of the escaping radiance

$$\alpha = \arccos(n \cdot \Omega). \tag{11}$$

The angle β is enclosed by the normal vector n and the outward direction Ω'' of the refracted light and is determined by means of *Snell's law*

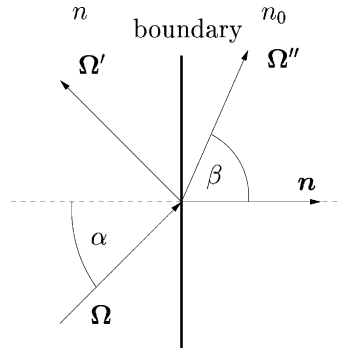Fig. 2. Relation between the outward directions $\boldsymbol{\Omega}$ and $\boldsymbol{\Omega}''$, and the inward direction $\boldsymbol{\Omega}'$ at the air–tissue interface. Light is reflected into the medium (refractive index n) along $\boldsymbol{\Omega}'$ and refracted along $\boldsymbol{\Omega}''$ when leaving the medium.

$$\beta = \arcsin\left(\frac{n\sin(\alpha)}{n_0}\right). \tag{12}$$

Total reflection ($R = 1$) is taken into account for $\beta > \pi/2$. As can be clearly seen, for a refractive index match ($n = n_0$) of both media at the interface we obtain the none-reentry boundary condition

$$\psi(\boldsymbol{\Omega}') = 0, \quad \boldsymbol{n} \cdot \boldsymbol{\Omega}' < 0. \tag{13}$$

2.3. Finite-difference discrete-ordinates method

Both transport equations, Eqs. (1) and (7), need to be solved numerically because no analytical solutions of the ERT are available for spatially heterogeneous media with finite geometrical boundaries [62]. Since the numerical solution method is the same for both transport equations, we will omit the superscript x and m in both equations for distinguishing the excitation and fluorescence field. We employ a finite-difference discrete-ordinates ($S_{\mathcal{N}}$) method that converts the integro-differential equation into a system of algebraic equations [62–71]. The radiance $\psi(\boldsymbol{r}, \boldsymbol{\Omega})$, which is a continuous function in space, is replaced by a finite set of H discrete radiances. The ERT is substituted by a set of approximate algebraic equations. The size of the algebraic system with its H unknown radiance values depends on the spatial (finite-difference) and angular (discrete-ordinates) discretization.

First, the direction $\boldsymbol{\Omega}$ is replaced with a set of discrete ordinates $\boldsymbol{\Omega}_k = (\xi_k, \eta_k, \mu_k)$ with *full level symmetry* [65,66,70,72]. The total number of ordinates $\boldsymbol{\Omega}_k$ with $k \in \{1..K\}$ is given by $K = \mathcal{N}(\mathcal{N} + 2)$ and $\mathcal{N}$ the number of direction cosines of the $S_{\mathcal{N}}$ method. The integral in the ERT is approximated with a quadrature rule

$$\int_{4\pi} p(\boldsymbol{\Omega} \cdot \boldsymbol{\Omega}')\psi(\boldsymbol{\Omega}', \boldsymbol{r})\mathrm{d}\boldsymbol{\Omega}' \approx \sum_{k'=1}^{K} w_{k'} p(\boldsymbol{\Omega}_k \cdot \boldsymbol{\Omega}_{k'})\psi(\boldsymbol{\Omega}_{k'}, \boldsymbol{r}) = \sum_{k'=1}^{K} w_{k'} p_{kk'} \psi_{k'}(\boldsymbol{r}) \tag{14}$$

where $w_{k'}$ are weights determined by full level symmetry of the ordinates [66]. The angular discretization yields a set of K coupled differential equations for the radiance $\psi(\boldsymbol{r}, \boldsymbol{\Omega}_k) = \psi_k(\boldsymbol{r})$ in the directions $\boldsymbol{\Omega}_k$:

$$\boldsymbol{\Omega}_k \cdot \nabla\psi_k(\boldsymbol{r}) + (\mu_a(\boldsymbol{r}) + \mu_s(\boldsymbol{r}))\psi_k(\boldsymbol{r}) = \mu_s(\boldsymbol{r}) \sum_{k'=1}^{K} w_{k'} p_{kk'} \psi_{k'}(\boldsymbol{r}) + S_k(\boldsymbol{r}). \tag{15}$$

The fluence $\phi(r)$ is obtained with

$$\phi(r) = \sum_{k=1}^{K} w_k \psi_k(r). \tag{16}$$

Next, the continuous spatial variable r is discretized on a three-dimensional Cartesian grid constituting a parallelepiped. Hence, the radiance $\psi_k(r)$ is only defined on grid points $r = (x_m, y_n, z_l)$ with $m \in \{1..M\}$, $n \in \{1..N\}$, and $l \in \{1..L\}$. The grid spacing between adjacent points is given by Δx, Δy, and Δz. We define for a given direction Ω_k and grid point (mnl) the radiance ψ_{mnlk}. The total number of unknown ψ_{mnlk} is $H = M \cdot N \cdot L \cdot K$.

Furthermore, the spatial derivatives $\nabla \psi_k(r) = (\partial \psi_k / \partial x, \partial \psi_k / \partial y, \partial \psi_k / \partial z)$ in Eq. (15) are substituted with first-order finite-difference approximations known as *step method* [65,66,70,73,74]. The difference formula of the step method depends on the direction Ω_k of the angular-dependent radiance ψ_{mnlk}. The set of all ordinates Ω_k for the unit sphere is subdivided into eight octants and we obtain eight different difference formulas for the radiance ψ_{mnlk}. For example, for all ordinates Ω_k with positive direction cosine $\xi_k > 0$ we have the following finite difference term along the x-axis

$$\frac{\partial \psi}{\partial x} \approx \frac{\psi_{mnl} - \psi_{m-1nl}}{\Delta x}. \tag{17}$$

The difference formula changes for negative direction cosine $\xi_k < 0$ and we obtain

$$\frac{\partial \psi}{\partial x} \approx \frac{\psi_{m+1nl} - \psi_{mnl}}{\Delta x}. \tag{18}$$

The same finite-difference approach is applied along the y-axis and z-axis for direction cosines η_k and μ_k. Hence, the discretized ERT for a grid point (mnl) is, for example, for all ordinates Ω_k within the octant $\xi_k > 0$, $\eta_k > 0$, and $\mu_k > 0$:

$$\xi_k \frac{\psi_{mnlk} - \psi_{m-1nlk}}{\Delta x} + \eta_k \frac{\psi_{mnlk} - \psi_{mn-1lk}}{\Delta y} + \mu_k \frac{\psi_{mnlk} - \psi_{mnl-1k}}{\Delta z} + ([\mu_s]_{mnl} + [\mu_a]_{mnl})\psi_{mnlk}$$

$$= [\mu_s]_{mnl} \sum_{k'=1}^{K} w_{k'} p_{kk'} \psi_{mnlk'} + S_{mnlk}. \tag{19}$$

Using the short-term notation $(\delta_x, \delta_y, \delta_z)$ for the discretized spatial derivative of $(\partial/\partial x, \partial/\partial y, \partial/\partial z)$ we obtain an algebraic system of equations for the discretized ERT for all grid points and ordinates

$$\{\xi_k \delta_x + \eta_k \delta_y + \mu_k \delta_z + [\mu_a]_{mnl} + [\mu_s]_{mnl}\}\psi_{mnlk} = [\mu_s]_{mnl} \sum_{k'=1}^{K} w_{k'} p_{kk'} \psi_{mnlk'} + S_{mnlk}. \tag{20}$$

The elements ψ_{mnlk} can be cast into a vector Ψ and we obtain in matrix notation

$$A\Psi = B\Psi + S, \tag{21}$$

with A as the discretized streaming and collision operator, B as the discretized integral operator or in-scatter term, and S as source term [68]. Furthermore, we introduce in Eq. (19) the vector notation [..] for all optical parameters that will be used in the remaining article. The nth element of a vector [..] is denoted by $[..]_n$.

2.4. Source iteration

We solve the system (21) for the radiance vector Ψ by employing a *source iteration* (SI) method [65,66,68,73]. This method is an iterative build-up of the radiance. By starting from an initial source term

($z = 0$), i.e. an external light source or an internal fluorescent source, an initial radiance vector Ψ^0 is computed as shown in Eq. (22)

$$A\Psi^0 = S. \tag{22}$$

The radiance Ψ^0 is now used to determine the in-scatter source term $B\Psi^0$ on the right hand side of Eq. (23). Since the right hand side for the next source iteration step ($z + 1$) is known from the previous step a new radiance vector Ψ^{z+1} can be determined

$$A\Psi^{z+1} = B\Psi^z + S. \tag{23}$$

A single iteration step for computing Ψ^{z+1} is also called *transport sweep*. The iteration process is repeated until the relative difference of the radiance of subsequent iteration steps is smaller than a predefined value κ given by the relation

$$\left| \frac{\Psi^{z+1} - \Psi^z}{\Psi^{z+1}} \right| < \kappa. \tag{24}$$

The radiance vector Ψ^Z of the last transport sweep Z is the solution of the discretized ERT. For example, at each transport sweep a single vector element ψ_{mnlk}^{z+1} for all ordinates $\boldsymbol{\Omega}_k$ with $\xi_k > 0$, $\eta_k > 0$, and $\mu_k > 0$ [see Eq. (19)] is calculated with

$$\psi_{mnlk}^{z+1} = \frac{S_{mnlk} + [\mu_s]_{mnl} \sum_{k'} w_{k'} p_{kk'} \psi_{mnlk'}^z + (\xi_k/\triangle x)\psi_{m-1nlk}^{z+1} + (\eta_k/\triangle y)\psi_{mn-1lk}^{z+1} + (\mu_k/\triangle z)\psi_{mnl-1k}^{z+1}}{(\xi_k/\triangle x) + (\eta_k/\triangle y) + (\mu_k/\triangle z) + [\mu_a]_{mnl} + [\mu_s]_{mnl}}. \tag{25}$$

According to the ERT at the excitation wavelength, see Eq. (1), the source term S_{mnlk} is the external light source S_{mnlk}^x. The optical parameters are $[\mu_a]_{mnl} = [\mu_a^{x\to}]_{mnl} + [\mu_a^{x\to m}]_{mnl}$, $[\mu_s]_{mnl} = [\mu_s^x]_{mnl}$. At the emission wavelength, see Eq. (7), we replace S_{mnlk} with the fluorescent source term $S_{mnlk}^m = (1/4\pi)\eta[\mu_a^{x\to m}]_{mnl}\phi_{mnl}^x$, and the optical parameters with $[\mu_a]_{mnl} = [\mu_a^m]_{mnl}$ and $[\mu_s]_{mnl} = [\mu_s^m]_{mnl}$.

2.5. Delta–Eddington method for highly anisotropically scattering media

A strongly anisotropic scattering phase function ($g > 0.7$) would require many discrete ordinates to suffice the normalization condition of the phase function in Eq. (4). Instead of using many discrete ordinates (e.g. S_{16} method with 288 ordinates) that increases the computational cost we employ a *Delta–Eddington* (DE) method. The DE method requires only, for example, an S_6 approximation with 48 ordinates for media with $g \approx 0.8$. In doing so, the scattering coefficient μ_s in both ERTs is replaced with

$$\mu_s^{DE} = (1 - g^3)\mu_s. \tag{26}$$

The Henyey–Greenstein function is also expanded into a series of Legendre polynomials up to second order and is replaced in both ERTs [Eqs. (1) and (7)]. More details of the DE method can be found in [75–77].

3. Inverse source problem

The inverse source problem derives the unknown spatial source distribution $S^m(\boldsymbol{r})$, which is proportional to the fluorophore absorption coefficient $\mu_a^{x\to m}(\boldsymbol{r})$ in Eq. (6), from the measured fluorescent light at wavelength λ^m escaping the tissue surface. Since the fluorophore absorption coefficient is a linear function of the fluorophore concentration inside the tissue a reconstructed map of the fluorophore absorption can directly be translated into a map of the concentration distribution of the biochemical probe. All other intrinsic tissue properties, i.e. the optical parameters $\mu_s^x(\boldsymbol{r})$, $\mu_s^m(\boldsymbol{r})$, $\mu_a^{x\to}(\boldsymbol{r})$, and $\mu_a^m(\boldsymbol{r})$, are typically given, for

example, from a previously performed reconstruction. Reconstruction algorithms in optical tomography for absorption and scattering coefficients are widely available and have been documented [53,54,56,78]. Furthermore, the quantum yield η of the fluorophore is also known and usually provided by the manufacturer.

3.1. Nonlinear optimization

The spatial distribution of the fluorophore absorption, $\mu_a^{x\to m}(r)$, is reconstructed by applying a nonlinear optimization technique to an objective function Φ that is an explicit function of $\mu_a^{x\to m}(r)$:

$$\Phi\left(\mu_a^{x\to m}(r)\right) := \varphi\left(\phi^m\left(\mu_a^{x\to m}(r)\right)\right). \tag{27}$$

The function $\varphi(\phi^m(r_d))$ describes the difference between the measured, $M^m(r_d)$, and predicted data, $\phi^m(r_d)$ [see Eq. (8)], at detector positions r_d for all D source–detector pairs

$$\varphi(\phi^m(r_d)) = \frac{1}{2} \sum_{d=1}^{D} \left(\frac{\phi^m(r_d) - M^m(r_d)}{\sigma^m(r_d)} \right)^2. \tag{28}$$

The quantity σ^m exhibits the confidence we have in the accuracy of our measurement data. It is largely influenced by the system noise of the experimental set-up that measures the light intensities at the tissue boundary. The main contribution to σ^m for an individual source–detector pair is the shot noise of a laser diode (source) and a charged-coupled-devices (CCD) camera (detector). Shot noise is a fundamental property of the quantum nature of light and varies according to a Poisson distribution. Its power is proportional to the square root of the measured signal $\sigma^m \sim \sqrt{M^m(r_d)}$.

We minimize the objective function by using a *limited-memory Broyden–Fletcher–Goldfarb–Shanno* (BFGS) technique that belongs to the class of quasi-Newton methods [56]. This technique updates iteratively an initial guess of the fluorophore absorption along a search direction. Once the minimum is found, the final result is the unknown distribution of the fluorophore absorption coefficients.

The updating procedure can be formulated as [79,80]

$$[\mu_a^{x\to m}]^{i+1} = [\mu_a^{x\to m}]^i + \alpha^i \boldsymbol{u}^i, \tag{29}$$

where $[\mu_a^{x\to m}]^i$ is a vector at iteration step i containing a set of fluorophore absorption coefficients $[\mu_a^{x\to m}]_{mnl}$ for all spatial grid points (*mnl*) from which the new vector $[\mu_a^{x\to m}]^{i+1}$ is obtained. The vector $\boldsymbol{u}^i$ is a search direction. The parameter α^i is the step length in the direction $\boldsymbol{u}^i$. After the update in Eq. (29) was performed a new search direction $\boldsymbol{u}^{i+1}$ is determined with [81,82]

$$\boldsymbol{u}^{i+1} = -\left[\frac{\mathrm{d}\Phi}{\mathrm{d}\mu_a^{x\to m}} \right]^{i+1} + \gamma \boldsymbol{s} + \lambda \boldsymbol{y} \tag{30}$$

with the vectors $\boldsymbol{s}$ and $\boldsymbol{y}$:

$$\boldsymbol{s} = \left[\mu_a^{x\to m}\right]^{i+1} - \left[\mu_a^{x\to m}\right]^i$$

$$\boldsymbol{y} = \left[\frac{\mathrm{d}\Phi}{\mathrm{d}\mu_a^{x\to m}} \right]^{i+1} - \left[\frac{\mathrm{d}\Phi}{\mathrm{d}\mu_a^{x\to m}} \right]^i. \tag{31}$$

The scalars γ and λ are defined by

$$\gamma = -\left(1 + \frac{\boldsymbol{y}^T \boldsymbol{y}}{\boldsymbol{s}^T \boldsymbol{y}} \right) \frac{\boldsymbol{s}^T [\mathrm{d}\Phi/\mathrm{d}\mu_a^{x\to m}]^{i+1}}{\boldsymbol{s}^T \boldsymbol{y}} + \frac{\boldsymbol{y}^T [\mathrm{d}\Phi/\mathrm{d}\mu_a^{x\to m}]^{i+1}}{\boldsymbol{s}^T \boldsymbol{y}}, \quad \lambda = \frac{\boldsymbol{s}^T [\mathrm{d}\Phi/\mathrm{d}\mu_a^{x\to m}]^{i+1}}{\boldsymbol{s}^T \boldsymbol{y}}. \tag{32}$$

At each iteration step i a new derivative $[\mathrm{d}\Phi/\mathrm{d}\mu_a^{x\to m}]^i$ needs to be calculated in order to determine the search direction $\boldsymbol{u}^i$. The derivative calculation is an essential part of the image reconstruction algorithm because it is computationally expensive. We have developed an adjoint differentiation method to compute the gradient. The details of this technique for the application in fluorescence tomography are described in the next section.

3.2. Adjoint differentiation

The optimization method requires calculating the derivative $[\mathrm{d}\Phi/\mathrm{d}\mu_a^{x\to m}]$ of the objective function that is a function of 10^3–10^5 variables $[\mu_a^{x\to m}]_{mnl}$ for all grid points (mnl). To approximate the derivative for a single variable $[\mu_a^{x\to m}]_{mnl}$ at grid point (mnl) we could apply the divided difference for a sufficiently small perturbation $\Delta\mu_a^{x\to m}$,

$$\left[\frac{\mathrm{d}\Phi}{\mathrm{d}\mu_a^{x\to m}}\right]_{mnl} \approx \frac{\Phi\big([\mu_a^{x\to m}]_{mnl} + \Delta\mu_a^{x\to m}\big) - \Phi\big([\mu_a^{x\to m}]_{mnl}\big)}{\Delta\mu_a^{x\to m}}. \tag{33}$$

This method, however, is computationally too expensive, since for each perturbation of $[\mu_a^{x\to m}]_{mnl}$ at grid point (mnl) a separate forward calculation has to be performed. That leads to a total of $(M\cdot N\cdot L + 1)$ forward calculations when all unknown fluorophore absorption coefficients are considered. Instead of perturbing each component of $[\mu_a^{x\to m}]$ we employ an adjoint method [83,84]. A particular implementation of that method is the adjoint differentiation technique [85–94]. We have already applied this technique to the image reconstruction problem of intrinsic tissue properties in optical tomography based on the ERT [55]. The adjoint differentiation method, also termed as computational or algorithmic differentiation in the reverse direction, is directly applied to the existing numerical code of the forward model. The main advantage of this approach is that the gradient can be calculated according to simple rules at a level of single steps in the forward code instead of solving an adjoint equation of radiative transfer that constitutes an entire new numerical problem [83,93,95,96]. Furthermore, the adjoint differentiation technique computes the derivative in a period of time equivalent to only one to three forward calculations.

The forward model of light propagation at wavelength λ^m, that provides a solution to the ERT [Eq. (7)] and a value of the objective function for a given fluorophore absorption distribution, is decomposed into a sequence of single differentiable functions. This sequence of functions is built up in the forward direction as the solution of the forward model is computed. Applying systematically the chain rule of differentiation to each single function in the reverse direction a numerical value of the derivative of the objective function with respect to the fluorophore absorption distribution is obtained.

3.2.1. Decomposition of the forward model

The adjoint differentiation approach exploits the algorithmic structure of the numerical forward model given by the source iteration scheme, see Eq. (23). The iterative build-up of the forward model calculates a sequence $(\Psi^0, \Psi^1, \ldots, \Psi^z, \ldots, \Psi^Z)$ of radiance distributions that converges towards a solution ψ^m of the ERT in Eq. (7). The radiance vector Ψ^{z+1} at the transport sweep $z+1$ is a function of the radiance vector Ψ^z at the previous transport sweep z and of a given fluorophore absorption $[\mu_a^{x\to m}]$. This function $\Psi^{z+1}(\Psi^z, [\mu_a^{x\to m}])$ is represented by the iteration rule in Eq. (25) for an individual vector element $[\Psi^{z+1}]_{mnlk}$. The final value Ψ^Z of the last transport sweep is used for the determination of the function

$$\varphi(\Psi^Z) = \frac{1}{2}\sum_{d=1}^{D}\frac{\left(\sum_k w_k \psi_{(d)k}^Z - M^m(\boldsymbol{r}_d)\right)^2}{M^m(\boldsymbol{r}_d)}, \tag{34}$$

where the subscript "d" pertains to a detector position r_d on the Cartesian mesh with grid point $(d) = (mnl)$. Thus, the objective function Φ, as defined in Eq. (27), is a composition of the function φ and Z functions Ψ^z of all transport sweeps:

$$\Phi = \left(\varphi \circ \Psi^Z \circ \Psi^{Z-1} \circ \cdots \circ \Psi^{z+1} \circ \Psi^z \circ \cdots \circ \Psi^1 \circ \Psi^0 \right). \tag{35}$$

The operation "$\circ$" is defined as a composite function

$$\Psi^{z+1} \circ \Psi^z = \Psi^{z+1}(\Psi^z, [\mu_a^{x \to m}]) \circ \Psi^z([\mu_a^{x \to m}]) := \Psi^{z+1}(\Psi^z([\mu_a^{x \to m}]), [\mu_a^{x \to m}]). \tag{36}$$

Starting with an initial input vector $[\mu_a^{x \to m}]$ a value of the objective function Φ can be obtained. That also defines the forward direction of the forward algorithm.

3.2.2. Algorithmic differentiation of the forward model

The derivative of the objective function Φ with respect to the input parameter of the forward algorithm, i.e. the fluorophore absorption vector $[\mu_a^{x \to m}]$, is given by the vector

$$\left[\frac{d\Phi}{d\mu_a^{x \to m}} \right] = \sum_{z=0}^{Z} \left[\frac{\partial(\varphi \circ \Psi^Z \circ \Psi^{Z-1} \circ \cdots \circ \Psi^z)}{\partial \mu_a^{x \to m}} \right]. \tag{37}$$

Each component of the above sum can be obtained by applying the chain rule of differentiation along the forward direction of the forward algorithm

$$\left[\frac{\partial(\varphi \circ \Psi^Z \circ \Psi^{Z-1} \circ \cdots \circ \Psi^z)}{\partial \mu_a^{x \to m}} \right] = \left[\frac{\partial \varphi}{\partial \Psi^Z} \right] \frac{\partial \Psi^Z}{\partial \Psi^{Z-1}} \frac{\partial \Psi^{Z-1}}{\partial \Psi^{Z-2}} \cdots \frac{\partial \Psi^{z+1}}{\partial \Psi^z} \frac{\partial \Psi^z}{\partial \mu_a^{x \to m}}. \tag{38}$$

Eq. (38) consists mainly of repeated matrix–matrix multiplications with $\partial \Psi^{z+1}/\partial \Psi^z$ and $\partial \Psi^z/\partial \mu_a^{x \to m}$ as matrices. The derivative $[\partial \varphi/\partial \mu_a^{x \to m}]$ is not included in the sum since φ is not an explicit function of $[\mu_a^{x \to m}]$ and thus its derivative vanishes.

We will now provide an algorithmic procedure that derives the gradient of Φ by applying systematically the chain rule of differentiation along the reverse direction of the forward algorithm in order to avoid repeated matrix–matrix multiplications. The algorithmic differentiation in the reverse direction requires only matrix–vector multiplications that leads to less computational effort. This procedure can be achieved by taking the transpose, or adjoint, of each component in (38)

$$\left[\frac{\partial(\varphi \circ \Psi^Z \circ \Psi^{Z-1} \circ \cdots \circ \Psi^z)}{\partial \mu_a^{x \to m}} \right]^T = \frac{\partial \Psi^z}{\partial \mu_a^{x \to m}}^T \frac{\partial \Psi^{z+1}}{\partial \Psi^z}^T \cdots \frac{\partial \Psi^{Z-1}}{\partial \Psi^{Z-2}}^T \frac{\partial \Psi^Z}{\partial \Psi^{Z-1}}^T \left[\frac{\partial \varphi}{\partial \Psi^Z} \right]^T. \tag{39}$$

Thus, we obtain with Eqs. (37) and (39)

$$\left[\frac{d\Phi}{d\mu_a^{x \to m}} \right]^T = \sum_{z=0}^{Z} \frac{\partial \Psi^z}{\partial \mu_a^{x \to m}}^T \left[\frac{\partial \Phi}{\partial \Psi^z} \right]^T. \tag{40}$$

Additionally, the relation between subsequent steps, $[\partial \Phi/\partial \Psi^z]^T$ and $[\partial \Phi/\partial \Psi^{z+1}]^T$, in Eq. (40) is for all $z < Z$,

$$\left[\frac{\partial \Phi}{\partial \Psi^z} \right]^T = \frac{\partial \Psi^{z+1}}{\partial \Psi^z}^T \left[\frac{\partial \Phi}{\partial \Psi^{z+1}} \right]^T, \tag{41}$$

and for $z = Z$,

$$\left[\frac{\partial \Phi}{\partial \Psi^Z} \right]^T = \left[\frac{\partial \varphi}{\partial \Psi^Z} \right]^T. \tag{42}$$

By providing the derivatives $[\partial\Phi/\partial\Psi^z]$, $\partial\Psi^z/\partial\mu_a^{x\rightarrow m}$, and $\partial\Psi^{z+1}/\partial\Psi^z$ for each transport sweep we are able to calculate the adjoint derivative vector $[d\Phi/d\mu_a^{x\rightarrow m}]^T$ in Eq. (40) by stepping through the forward algorithm in the reverse direction. Starting with the last transport sweep we compute the partial derivative in Eq. (42) by differentiating Eq. (34) and obtain for each component at detector position r_d:

$$\frac{\partial\Phi}{\partial\psi_{(d)k}^Z} = \frac{\partial\varphi}{\partial\psi_{(d)k}^Z} = \frac{\left(\sum_k w_k\psi_{(d)k}^Z - M^m(r_d)\right)}{M^m(r_d)}w_k. \tag{43}$$

Next, the derivative of ψ_{mnlk}^z with respect to $[\mu_a^{x\rightarrow m}]_{mnl}$ in Eq. (40) is given by

$$\frac{\partial\psi_{mnlk}^z}{\partial[\mu_a^{x\rightarrow m}]_{mnl}} = \frac{(1/4\pi)\eta\phi_{mnl}^x}{(\xi_k/\triangle x) + (\eta_k/\triangle y) + (\mu_k/\triangle z) + [\mu_a^m]_{mnl} + [\mu_s^m]_{mnl}}. \tag{44}$$

Finally, the matrix components in Eq. (41) are given by the partial derivatives

$$\frac{\partial\psi_{mnlk}^{z+1}}{\partial\psi_{m'n'l'k'}^z} = \left\{[\mu_s^m]_{mnl}w_{k'}p_{kk'}\delta_{mm'nn'll'} + \frac{\xi_k}{\triangle x}\frac{\partial\psi_{m-1nlk}^{z+1}}{\partial\psi_{m'n'l'k'}^z} + \frac{\eta_k}{\triangle y}\frac{\partial\psi_{mn-1lk}^{z+1}}{\partial\psi_{m'n'l'k'}^z} + \frac{\mu_k}{\triangle z}\frac{\partial\psi_{mnl-1k}^{z+1}}{\partial\psi_{m'n'l'k'}^z}\right\}$$
$$\left/ \left\{\frac{\xi_k}{\triangle x} + \frac{\eta_k}{\triangle y} + \frac{\mu_k}{\triangle z} + [\mu_s^m]_{mnl} + [\mu_a^m]_{mnl}\right\}\right. \tag{45}$$

with

$$\delta_{mm'nn'll'} = \delta_{mm'}\delta_{nn'}\delta_{ll'} \quad \text{and} \quad \delta_{aa'} = \begin{cases} 1 & \text{if } a' = a \\ 0 & \text{if } a' \neq a. \end{cases}$$

We also approximate the partial derivatives on the right-hand-side in Eq. (45) with

$$\frac{\partial\psi_{m-1nlk}^{z+1}}{\partial\psi_{m'n'l'k'}^z} := \delta_{(m-1)m'nn'll'kk'}$$
$$\frac{\partial\psi_{mn-1lk}^{z+1}}{\partial\psi_{m'n'l'k'}^z} := \delta_{mm'(n-1)n'll'kk'} \tag{46}$$
$$\frac{\partial\psi_{mnl-1}^{z+1}}{\partial\psi_{m'n'l'k'}^z} := \delta_{mm'nn'(l-1)l'kk'}$$

since ψ_{m-1nlk}^{z+1}, ψ_{mn-1lk}^{z+1}, and ψ_{mnl-1k}^{z+1} are slowly varying functions of $\psi_{m'n'l'k'}^z$ for sufficiently small Δx, Δy, and Δz. We found that in general the error introduced by this approximation is negligible.

The differentiation of the objective function along the reverse direction of the forward algorithm constitutes a computational advantage over the differentiation along the forward direction. In the reverse direction a matrix always operates on a vector [see Eq. (39)]. For example, multiplication of a squared matrix with size of q^2 elements and a vector with q elements involves a total of $2q^2 - q$ operations (q multiplications and $q - 1$ summations for each new vector element). However, by calculating the derivative in the forward direction [see Eq. (38)] a matrix operates on a matrix. A matrix–matrix multiplication requires a total of $2q^3 - q^2$ operations (q multiplications and $q - 1$ summations for each new matrix element). Since matrix–vector multiplications consist of q times fewer operations than matrix–matrix multiplications computing the derivative along the reverse direction involves less computational effort and is q times faster.

4. Inverse problem of total absorption

Besides $\mu_a^{x\rightarrow m}(r)$ of the fluorophore the total absorption coefficient $\mu_a^x(r) = \mu_a^{x\rightarrow}(r) + \mu_a^{x\rightarrow m}(r)$ at the excitation wavelength λ^x can be reconstructed to provide information about the intrinsic tissue and fluorophore absorption. In this case we define an objective function, $\Phi(\mu_a^x(r)) = \varphi(\phi^x(\mu_a^x(r)))$, similar to Eq. (28) as

$$\varphi(\phi^{x}(\mathbf{r}_d)) = \frac{1}{2} \sum_{d=1}^{D} \frac{(\phi^{x}(\mathbf{r}_d) - M^{x}(\mathbf{r}_d))^2}{M^{x}(\mathbf{r}_d)}. \tag{47}$$

The predicted detector readings $\phi^{x}(\mathbf{r}_d)$ are calculated by solving the ERT in Eq. (1). The measurement data $M^{x}(\mathbf{r}_d)$ are given at the excitation wavelength λ^{x}. The objective function $\Phi(\mu_{a}^{x}(\mathbf{r}))$ is iteratively minimized by using the nonlinear optimization method to find the unknown distribution of absorption coefficients $\mu_{a}^{x}(\mathbf{r})$. Again, we employ the adjoint differentiation technique applied to the forward algorithm of Eq. (1) to provide the derivative vector of Φ with respect to $[\mu_{a}^{x}]$.

The derivative vector $[\mathrm{d}\Phi/\mathrm{d}\mu_{a}^{x}]$ is computed in the same manner as explained in Section 3.2. Eq. (40) is modified and we obtain

$$\left[\frac{\mathrm{d}\Phi}{\mathrm{d}\mu_{a}^{x}}\right]^{\mathrm{T}} = \sum_{z=0}^{Z} \frac{\partial \Psi^{z\mathrm{T}}}{\partial \mu_{a}^{x}} \left[\frac{\partial \Phi}{\partial \Psi^{z}}\right]^{\mathrm{T}}. \tag{48}$$

Again, Eq. (41) as applied to ERT I is used for calculating the subsequent step $[\partial\Phi/\partial\Psi^{z}]^{\mathrm{T}}$ from $[\partial\Phi/\partial\Psi^{z+1}]^{\mathrm{T}}$ in the reverse direction. A matrix element of $\partial\Psi^{z}/\partial\mu_{a}^{x}$ in Eq. (48) is

$$\frac{\partial \psi_{mnlk}^{z}}{\partial [\mu_{a}^{x}]_{mnl}} = -\frac{S_{mnlk}^{x} + [\mu_{s}^{x}]_{mnl} \sum_{k'} w_{k'} p_{kk'} \psi_{mnlk'}^{z-1}}{\left(\frac{\xi_k}{\triangle x} + \frac{\eta_k}{\triangle y} + \frac{\mu_k}{\triangle z} + [\mu_{a}^{x}]_{mnl} + [\mu_{s}^{x}]_{mnl}\right)^2} - \frac{\frac{\xi_k}{\triangle x}\psi_{m-1nlk}^{z} + \frac{\eta_k}{\triangle y}\psi_{mn-1lk}^{z} + \frac{\mu_k}{\triangle z}\psi_{mnl-1k}^{z}}{\left(\frac{\xi_k}{\triangle x} + \frac{\eta_k}{\triangle y} + \frac{\mu_k}{\triangle z} + [\mu_{a}^{x}]_{mnl} + [\mu_{s}^{x}]_{mnl}\right)^2}. \tag{49}$$

5. Experimental results

In the following section we show the first experimental results of recovering the spatial distribution of fluorescent sources in a tissue-like phantom using the transport-theory based reconstruction code. Experimental data were recorded at both the excitation and emission wavelengths in order to reconstruct the total absorption, $\mu_{a}^{x} = \mu_{a}^{x\rightarrow} + \mu_{a}^{x\rightarrow m}$, and fluorophore absorption, $\mu_{a}^{x\rightarrow m}$. The instrumental design we used for acquiring the experimental data are described in more detail by Graves et al. [97].

The given tissue-like phantom had a size of 4 cm × 4 cm × 1.3 cm with the optical parameters $\mu_{s}^{x} = 30$ cm^{-1} and $\mu_{a}^{x\rightarrow} = 0.4$ cm^{-1} at the excitation wavelength, and $\mu_{s}^{m} = 30$ cm^{-1} and $\mu_{a}^{m} = 0.4$ cm^{-1} at the emission wavelength, see Fig. 3. The refractive index of the phantom was $n = 1.33$. The anisotropy factor was assumed to be $g = 0.8$. The highly forward-peaked scattering phase function and the use of an S_6 method with only 48 ordinates required the DE method to suffice the normalization condition [Eq. (4)]. Hence, the scattering coefficient for both wavelengths was rescaled with relation (26) that yielded
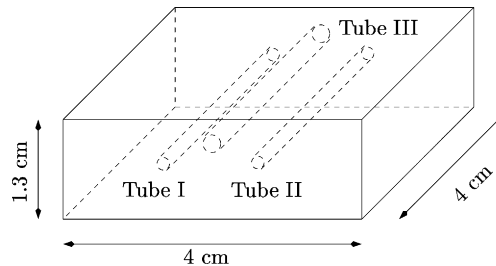

Fig. 3. Scattering phantom with three embedded tubes. Tubes I and II contained a fluorochrome with $\mu_{a}^{x\rightarrow m} < \mu_{a}^{x}$ of background medium. Tube III is purely absorbing and had a higher absorption than the background medium.

$\mu_s^{DE} = 14.64$ cm^{-1}. All forward calculations and reconstructions were performed on a $41 \times 41 \times 14$ grid with spatial separation $\Delta x = \Delta y = \Delta z = 0.1$ cm.

Two fluorescent tubes (I and II) with a diameter of 0.2 cm were embedded inside the medium at depths $d_I = 0.55$ cm and $d_{II} = 0.55$ cm, measured from the top plane of the phantom ($d = 0$ cm). Both tubes contained a fluorochrome (Cy5.5 Amersham Pharmacia Biotech, NJ, USA) that pertains to the group of carbocyanine dyes [12]. This fluorescent dye had an extinction coefficient $\epsilon = 250{,}000$ M^{-1}cm^{-1} and a quantum yield $\eta = 0.28$. The concentration inside the tubes was $c = 2 \times 10^{-7}$ M yielding a fluorophore absorption $\mu_a^{x \to m} = 0.05$ cm^{-1}. The intrinsic absorption was $\mu_a^{x \to} = 0$ cm^{-1} and same scattering properties as background medium were present.

Additionally, an absorbing tube (III) with a diameter of 0.3 cm and no fluorescent properties was included at depth $d_{III} = 0.3$ cm. This tube had an increased absorption coefficient with respect to the background medium.

Thirty-two source fibers were placed on the bottom plane of the phantom ($d = 1.3$ cm) on an area of 1.2×1.8 cm^2, and 150 equally distributed detector points were on the top plane ($d = 0$ cm) on an area of 1.9×2.5 cm^2. The source fibers illuminated the phantom at the excitation wavelength $\lambda^x = 675$ nm. The light propagation model took the partially collimated light source with an aperture $\approx \pi/3$ into account by assigning a non-zero source power density $S(\mathbf{\Omega}_k) > 0$ to only four ordinates that pointed inside the medium. The escaping light at the detection plane was recorded at the excitation and fluorescent wavelength ($\lambda^m = 694$ nm) using wavelength selective filters and a CCD camera. We obtained a tomographical data set with $D = 32 \times 150$ source–detector pairs.

In the next sections we show the reconstructed fluorophore absorption distribution and the total absorption distribution by employing measurement data sets at either the fluorescence wavelength, the excitation wavelength, or at both wavelengths.

5.1. Fluorophore absorption reconstruction using measurement data at fluorescent wavelength λ^m

Given the experimental set-up we independently measured for 32 sources the fluorescent light that escaped the top plane of the medium. The measured data became input to the image reconstruction algorithm. The optimization process started from an initial guess $[\mu_a^{x \to m}]^0 = 0$ cm^{-1}. The optimization was stopped when the relative difference $|(\Phi^{i+1} - \Phi^i)/\Phi^i|$ of the objective function between two consecutive iteration steps became smaller than 10^{-8}. It took 28 iterations with 28 adjoint derivative and 33 forward calculations for each source position. One complete forward calculation comprised solving the ERT for all 32 source positions. Hence, one complete adjoint derivative calculation involved the solution of the ERT for all source positions of the forward code. Therefore, the reconstruction time was approximately 25 h on a *Linux Beowulf Cluster* consisting of 10 *Intel Pentium III Xeon* processors with 2.4 GHz clock rate. The reconstructed fluorophore distribution $\mu_a^{x \to m}(\mathbf{r})$ is shown in Fig. 4. In this case it was not possible to derive quantitative information about the fluorophore distribution due to the unknown source strength at the excitation wavelength λ^x. Therefore, we display in Fig. 4 a relative fluorophore absorption coefficient distribution with arbitrary units. The relative fluorophore absorption distribution is normalized to its maximum value. Thus, the image scale is 0...1 with maximum fluorophore absorption at 1 and no fluorophore absorption at 0.

5.2. Fluorophore absorption reconstruction using measurement data at fluorescent wavelength λ^m and excitation wavelength λ^x

Absolute values of the measured light intensity at the fluorescent wavelength λ^m need to be accessible for a given excitation source strength at λ^x to reconstruct the absolute fluorophore absorption distribu-
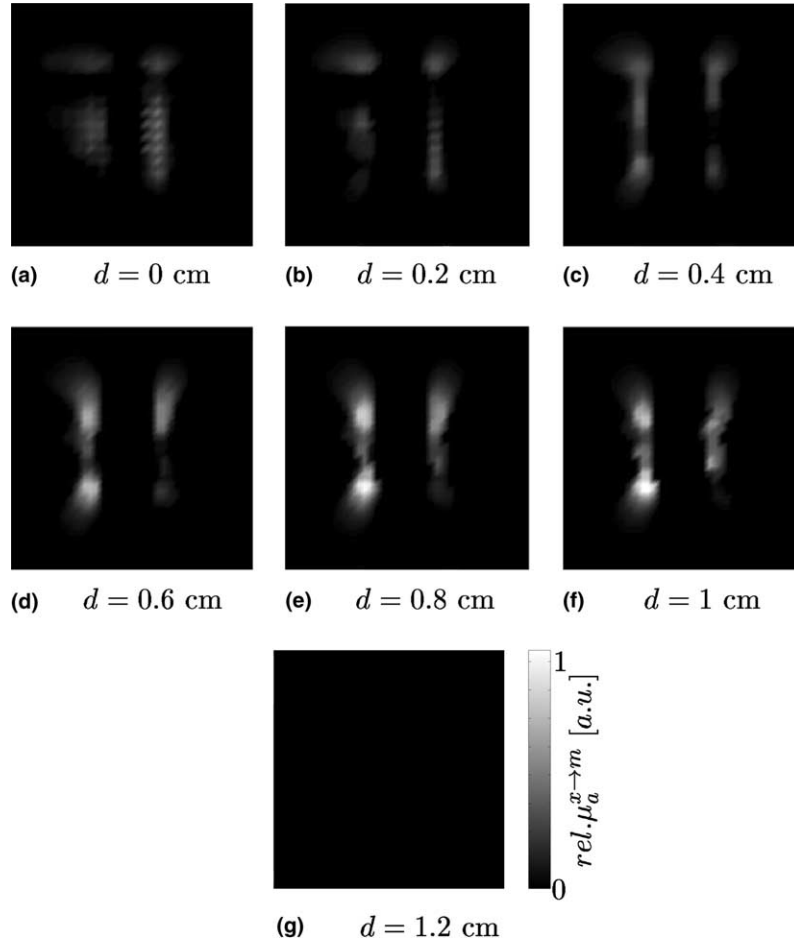
Fig. 4. Reconstructed relative fluorophore absorption $\mu_a^{x \to m}$ in different depths d measured from top plane ($d = 0$ cm). The fluorophore distribution is normalized to its maximum value. The excitation sources were located at $d = 1.3$ cm and the detector plane for measuring the fluorescent light was located at $d = 0$ cm. Both fluorescent tubes (Tube I and II) can be clearly seen.

tion. However, the experimental situation does often not allow to determine the absolute fluorescent light intensity, e.g. due to unknown excitation source strengths, unknown filter attenuation and fiber coupling coefficients, and unknown losses at the tissue–air interfaces [44,45,48,98,99]. These quantities can be described by a re-scaling factor that depends on the particular experimental set-up. This re-scaling factor can be obtained by relating measured light intensities $\tilde{M}_0^x$ at the excitation wavelength λ^x for the homogeneous phantom with known optical properties without any tubes present to numerically predicted light intensities ϕ_0^x for the same medium. The measured fluence $\tilde{M}^m$ at the emission wavelength λ^m for the phantom with the unknown fluorophore distribution is re-scaled by that factor which is defined as the ratio $\phi_0^x / \tilde{M}_0^x$. Hence, the re-scaled measurement data M^m at detector positions $\boldsymbol{r}_d$ are given by the relation

$$M^m(\boldsymbol{r}_d) = \frac{\tilde{M}^m(\boldsymbol{r}_d) \cdot \phi_0^x(\boldsymbol{r}_d)}{\tilde{M}_0^x(\boldsymbol{r}_d)}, \tag{50}$$

and are independent of all experimental design-dependent light intensity losses. Subsequently, the re-scaled measurement data $M^m(r_d)$ became input to the objective function (28) of the image reconstruction algorithm. A similar re-scaling approach is described elsewhere [44,45,48].

The reconstructed fluorophore absorption $\mu_a^{x \to m}$ is shown in Fig. 5. The images show the positions of the fluorescent tubes I and II. The maximum value of the reconstructed fluorophore absorption distribution is $\mu_a^{x \to m} = 0.032$ cm^{-1}. The fluorophore absorption $\mu_a^{x \to m}$ was reconstructed starting from a homogeneous initial guess $[\mu_a^{x \to m}]^0 = 0$ cm^{-1}. The reconstruction process was terminated when the relative difference $|(\Phi^{i+1} - \Phi^i)/\Phi^i|$ of subsequent iteration steps of the optimization process was smaller than 5×10^{-4}. The optimization technique needed 23 iterations that included a total of 35 forward calculations and 23 adjoint derivative calculations. The computation time was approximately 21 h.

5.3. Total absorption reconstruction using measurement data at excitation wavelength λ^x

The spatial distribution of the total absorption coefficient $\mu_a^x = \mu_a^{x \to} + \mu_a^{x \to m}$ was reconstructed given the experimental measurement data at excitation wavelength λ^x. Again, we needed to re-scale the measurement data $\tilde{M}^x(r_d)$ due to the unknown light intensity losses of the experimental design:

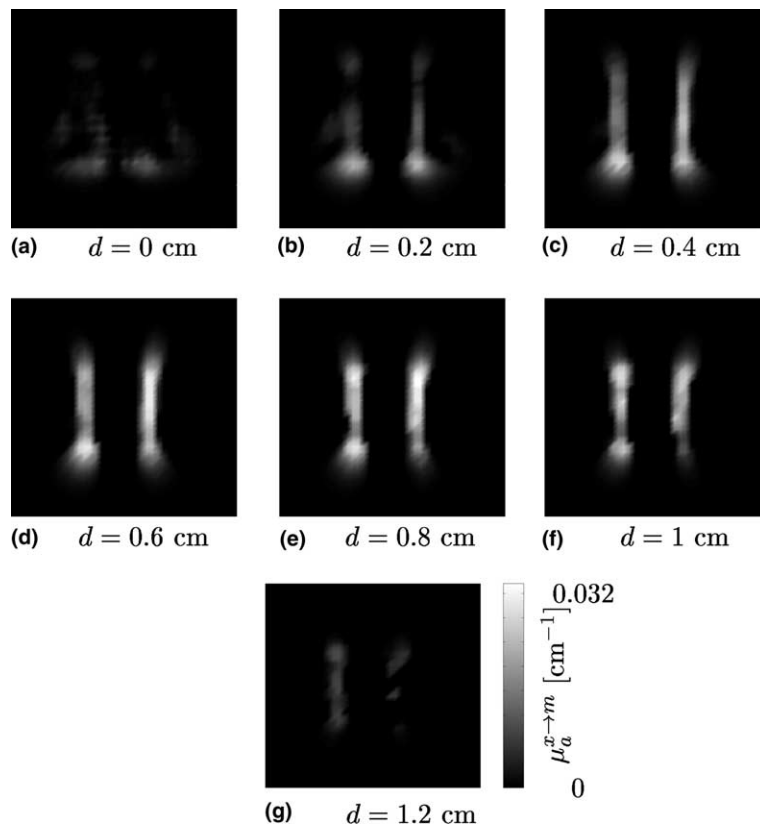Fig. 5. Reconstructed fluorophore absorption $\mu_a^{x \to m}$ in different depths d measured from top plane ($d = 0$ cm). The excitation sources were located at $d = 1.3$ cm. The excitation and fluorescent light intensities were measured at the detector positions in the top plane at $d = 0$ cm. Both fluorescent tubes (Tube I and II) can be clearly seen.

$$M^x(\mathbf{r}_d) = \frac{\tilde{M}^x(\mathbf{r}_d) \cdot \phi_0^x(\mathbf{r}_d)}{\tilde{M}_0^x(\mathbf{r}_d)}. \tag{51}$$

The re-scaled measurement data $M^x(\mathbf{r}_d)$ became input to the objective function [see also Eq. (47)] of the reconstruction algorithm.

The image reconstruction started from an initial guess $[\mu_a^x]^0 = 0.4$ cm^{-1}. The stop criterion was set to $|(\Phi^{i+1} - \Phi^i)/\Phi^i| < 10^{-2}$. The reconstruction process was finished after 58 iterations with a total of 58 forward and 58 adjoint derivative calculations. The computation time was approximately 40 h. All reconstructed images for different depths measured from the top plane of the phantom are shown in Fig. 6.

All three tubes (I, II, and III) can be seen in the images. The central tube (III) is the highly absorbing tube that contains no fluorophore and has a higher absorption coefficient than the background medium. Its maximum value of absorption is $\mu_a^x = 1.29$ cm^{-1} at depth $d = 0.4$ cm. Both fluorescent tubes, I and II, have an absorption coefficient $\mu_a^x < 0.1$ cm^{-1} smaller than the background medium in tomographic plane $d = 0.6$ cm.
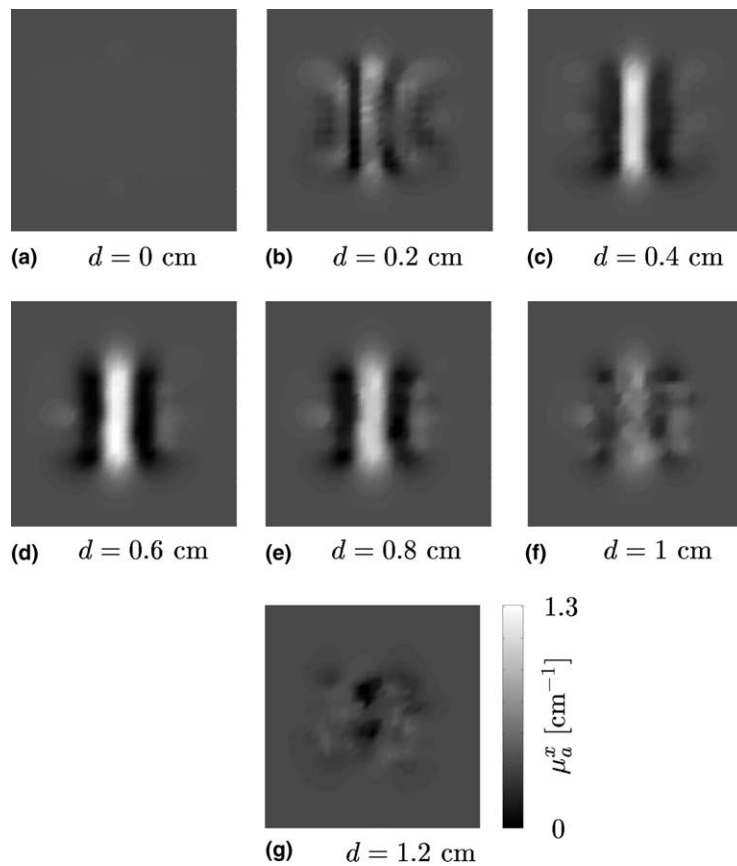

Fig. 6. Reconstructed total absorption μ_a^x in different depths d measured from top plane ($d = 0$ cm). The background medium has an absorption of $\mu_a^x = 0.4$ cm^{-1}. The excitation sources were located at $d = 1.3$ cm and the detectors were located at $d = 0$ cm. Both fluorescent tubes (I and II) can be seen as dark areas with a low absorption $\mu_a^x < 0.1$ cm^{-1} due to the fluorophore. The purely absorbing tube (III) with $\mu_a^x > 1$ cm^{-1} is present in the center as a white elongated area.

6. Discussion and summary

We have developed a reconstruction algorithm for recovering the spatial distribution of fluorescent sources in highly scattering media. The code provides tomographic images of the fluorophore absorption coefficient that can be used in molecular imaging of biological tissue. The presented reconstruction algorithm includes two original aspects that have not been used before in fluorescence tomography.

First, the forward model for light propagation is based on the ERT and not the widely employed diffusion approximation. By not relying on the diffusion approximation, this algorithm has the potential to provide more accurate solutions in cases where the diffusion approximation fails, such as in media with small geometries, media with high absorption coefficients, or small source–detector separations. Having provided an ERT-based reconstruction code we are now in the position to quantify the advantages in future studies.

Second, an adjoint differentiation method for fluorescence tomography has been developed. This method is used to compute the derivative of an objective function to provide search directions for the nonlinear optimization technique. By applying the chain rule of differentiation to all transport sweeps of the forward algorithm the derivative can be built up in an iterative manner. The chain rule can be executed in two different ways, either in the forward direction or reverse direction of the numerical code of the light propagation model. By applying the chain rule of differentiation in the forward direction matrix–matrix multiplications need to be performed for all transport sweeps as can be seen in Eq. (38). On the other hand, in the reverse or adjoint direction, as shown by Eqs. (40) and (41), only matrix–vector multiplications are necessary that considerably decreases the amount of computational operations. The adjoint differentiation technique has also the advantage that the existing code of the forward model can be utilized to compute the derivative. A numerical implementation of an adjoint ERT as shown, for example, by Ustinov et al. [95] is not required.

In general, the tomographic images calculated from experimental measurement data show a qualitatively accurate distribution of the fluorophore absorption coefficient [Figs. 4 and 5] and the total absorption coefficient [Fig. 6]. The fluorescent tubes I and II can clearly be resolved with the original diameters of 0.2 cm in a tomographic plane for a specific depth d. The depth resolution is not as good since detectors were only placed on the top plane opposite to the sources. In order to obtain a better depth resolution the medium needs to be illuminated and the escaping light needs to be measured from different views. We further observe that the resolution of the fluorescent images is higher than the images of the total absorption. We still notice image artifacts close to the detector plane ($d \approx 0.1$ cm) and to the source plane ($d \approx 1.3$ cm) as can be seen, for example, in Fig. 5. These artifacts are most likely caused by the high sensitivity of the objective function with respect to changes in the fluorophore absorption coefficient in the vicinity of source and detector points.

We used two different types of measurement data for reconstructing the fluorophore absorption distribution. First, only measurement data at the emission wavelength were employed, and second, measurement data at the emission and excitation wavelengths were used. In the first case, the image reconstruction method was able to reconstruct qualitatively the fluorophore absorption distribution. The tomographic images in Fig. 4 show both fluorescent tubes with a significantly higher light emission than the background medium. However, no quantitative information, i.e. the absolute fluorophore absorption coefficient, could be retrieved because of unknown excitation source strengths and unknown intensity losses at the tissue–air interface. Quantitative information of $\mu_a^{x \to m}(\mathbf{r})$ may still be obtained by using a set of reference solutions with well-known concentrations of *Cy5.5*. Furthermore, our reconstruction results show that all numerical approximations and assumptions made within the light propagation model (step method, S_6 approximation, DE method) and within the optimization process (using approximate partial derivatives for the adjoint differentiation, uncertainty of intrinsic optical parameters) have relatively little impact on the qualitative image reconstruction. On the other hand, the reconstructed images are noisier when compared to images in Fig. 5 that uses re-scaled measurement data. That is

mostly due to the unknown intensity losses which is dependent on each individual source and detector point position.

In the second case, where measurements at the emission and excitation wavelengths are used, the uncertainties of unknown intensity losses can be overcome. This is achieved by re-scaling the measurements at λ^m prior to reconstruction with measurements at λ^x taken from the homogeneous medium. In this way we could reconstruct images with little noise as shown in Fig. 5. Besides that, we were also able to determine the absolute fluorophore absorption coefficient. That enables us to derive the fluorophore and molecular probe concentration for a future small animal imaging system without employing reference solutions of *Cy5.5*. Another important characteristic of using re-scaled measurement data are that it may correct shortcomings of the used light propagation model. For example, the reconstruction method may be less prone to errors introduced by a coarse spatial Cartesian grid or errors caused by ray-effects and false scattering [69,100]. In contrast, a reconstruction code that uses re-scaled measurement data may not be able to model correctly light propagation in physical domains where the same code might work when unprocessed data are used.

Besides the distribution of the fluorophore absorption $\mu_a^{x \to m}$, we can also reconstruct the total absorption distribution $\mu_a^x = \mu_a^{x \to} + \mu_a^{x \to m}$ as illustrated in Fig. 6 that shows all three tubes. This example is of particular interest, because it deals with a non-diffusive regime. In Tube III the absorption coefficient ($\mu_a^x > 1$ cm^{-1}) is approximately six times smaller than the reduced scattering coefficient $\mu_s'^x = (1 - g)\mu_s^x = 6$ cm^{-1} of the background medium. Hielscher et al. [101] have shown that the diffusion model inaccurately describes light propagation in this domain.

Despite the ill-posedness of the inverse source problem we still achieve quite accurate reconstruction results. In our example we have an underdetermined inverse problem with 23,534 unknowns but only 4800 measurement data. That we nevertheless get reasonable results may be explained by two major aspects. First, only 1.21% of the phantom's volume contained fluorophores with a fluorophore absorption coefficient $\mu_a^{x \to m}$ larger than zero. The remaining phantom volume (98.79%) had no fluorescent properties with $\mu_a^{x \to m} = 0$ cm^{-1}. Since we started the optimization process from an initial guess $[\mu_a^{x \to m}]^0 = 0$ cm^{-1} we assigned to most of the unknown fluorophore absorption coefficients the correct value. This is a reasonable approach, as this mimics the practical situation. In practice, an administered fluorescent molecular probe will mainly accumulate in the side of interest, while the rest of the tissue will not show increased levels of fluorophore concentration. Therefore, an initial guess of $[\mu_a^{x \to m}]^0 = 0$ cm^{-1} for the entire medium will provide an initial guess close to the true solution, which will often result in a satisfactory convergence of the optimization process.

Second, due to the source–detector configuration of the experimental set-up we have a limited field of view (FOV). Consequently, the objective function is most sensitive to a fluorophore absorption distribution within a phantom volume that is enclosed by the source area (2.16 cm^2) and detector area (4.75 cm^2) on the bottom and top plane of the phantom. The enclosed volume with approximately 7000 unknown fluorophore absorption coefficients only accounts for 30% of the entire phantom volume. Fluorophore absorption coefficients $\mu_a^{x \to m}$ outside of the targeted volume do not or only little contribute to the overall sensitivity $d\Phi/d\mu_a^{x \to m}$ of the objective function Φ. Hence, the inverse source problem becomes less underdetermined.

The presence of measurement noise and a model error prohibit the uniqueness of the inverse problem. A comprehensive uncertainty analysis, that describes the impact of the measurement error on the image error, has not been performed yet, neither for transport-theory-based reconstruction methods nor for the widely applied diffusion-theory-based reconstruction methods. In the future, other approaches could be considered to decrease the ill-posedness. For example, some researchers employ different regularization methods such as Tikhonov regularization; or the inverse source problem can also be formulated within a *Bayesian* framework that allows the incorporation of *prior* knowledge and uses all available information about the problem model (forward and inverse model) within the objective function [48].

Acknowledgments

This work was supported in part by a postdoctoral fellowship awarded to Dr. Klose from the Ernst Schering Research Foundation, Germany, and a grant from the National Institute of Biomedical Imaging and Bioengineering (5 R33 CA 91807-3), which is part of the National Institutes of Health. We also thank Dr. Gassan Abdoulaev (Department of Biomedical Engineering, Columbia University) and Dr. Guillaume Bal (Department of Applied Mathematics, Columbia University) for helpful comments reviewing this paper.

References

[1] R. Weissleder, U. Mahmood, Molecular imaging, Radiology 219 (2001) 316.
[2] P.R. Contag, Whole-animal cellular and molecular imaging to accelerate drug development, Drug Discovery Today 7 (2002) 555.
[3] R.J. Gillies, In vivo molecular imaging, J. Cell. Biochem. Suppl. 39 (2002) 231.
[4] T.F. Massoud, S.S. Gambhir, Molecular imaging in living subjects: seeing fundamental biological processes in a new light, Genes Dev. 17 (2003) 545.
[5] R.G. Blasberg, Molecular imaging and cancer, Mol. Cancer Therap. 2 (2003) 335.
[6] R.G. Blasberg, J.G. Tjuvajev, Molecular-genetic imaging: current and future perspectives, J. Clin. Invest. 111 (2003) 1620.
[7] S.R. Cherry, In vivo molecular imaging and genomic imaging: new challenges for imaging physics, Phys. Med. Biol. 49 (2004) R13.
[8] D. Piwnica-Worms, D.P. Schuster, J.R. Garbow, Molecular imaging of host-pathogen interactions in intact small animals, Cell. Microbiol. 6 (2004) 319.
[9] J. Allport, R. Weissleder, In vivo imaging of gene and cell therapies, Exp. Hematol. 29 (2001) 1237.
[10] C. Bremer, V. Ntziachristos, R. Weissleder, Optical-based molecular imaging: contrast agents and potential medical applications, Eur. Radiol. 13 (2001) 231.
[11] D.J. Bornhop, C.H. Contag, K. Licha, C.J. Murphy, Advances in contrast agents, reporters, and detection, J. Biomed. Opt. 6 (2001) 106.
[12] K. Licha, Contrast agents for optical imagingTopics in Current Chemistry, vol. 222, Springer, Heidelberg, 2002, pp. 1–29.
[13] R. Weissleder, V. Ntziachristos, Shedding light onto live molecular targets, Nat. Med. 9 (2003) 123.
[14] G. Choy, P. Choyke, S.K. Libutti, Current advances in molecular imaging: noninvasive in vivo bioluminescent and fluorescent optical imaging in cancer research, Mol. Imaging 2 (2003) 303.
[15] J.E. Bugaj, S. Achilefu, R.B. Dorshow, R. Rajagopalan, Novel fluorescent contrast agents for optical imaging of in vivo tumors based on a receptor-targeted dye-peptide conjugate platform, J. Biomed. Opt. 6 (2001) 122.
[16] A. Becker, C. Hessenius, K. Licha, B. Ebert, U. Sukowski, W. Semmler, B. Wiedenmann, C. Grötzinger, Receptor-targeted optical imaging of tumors with near-infrared fluorescent ligands, Nat. Biotechnol. 19 (2001) 327.
[17] C.J. Daly, J.C. McGrath, Fluorescent ligands, antibodies, and proteins for the study of receptors, Pharmacol. Therap. 100 (2003) 101.
[18] R. Weissleder, C.-H. Tung, U. Mahmood, A. Bogdanov, In vivo imaging of tumors with protease-activated near-infrared fluorescent probes, Nat. Biotechnol. 17 (1999) 375.
[19] V. Ntziachristos, C.H. Tung, C. Bremer, R. Weissleder, Fluorescence molecular tomography resolves protease activity in vivo, Nat. Med. 8 (2002) 757.
[20] V. Ntziachristos, R. Bremer, R. Weissleder, Fluorescence imaging with near-infrared light: new technological advances that enable in vivo molecular imaging, Eur. Radiol. 13 (2003) 195.
[21] P. Wunderbaldiger, A. Bogdanov, R. Weissleder, New approaches for imaging in gene therapy, Eur. J. Radiol. 34 (2000) 156.
[22] B.W. Rice, M.D. Cable, M.B. Nelson, In vivo imaging of light-emitting probes, J. Biomed. Opt. 6 (2001) 432.
[23] Y. Chen, G. Zheng, Z.H. Zhang, D. Blessington, M. Zhang, H. Li, Q. Liu, L. Zhou, X. Intes, S. Achilefu, B. Chance, Metabolism-enhanced tumor localization by fluorescence imaging: in vivo animal studies, Opt. Lett. 28 (2003) 2070.
[24] F. Natterer, Mathematical models for medical imaging, in: Ch. Boergers, F. Natterer (Eds.), Computational Radiology and Imaging: Therapy and Diagnostics. The IMA Volumes in Mathematics and its Applications, Springer, New York, 1999, pp. 17–32.
[25] N.J. McCormick, Inverse radiative transfer problems: a review, Nucl. Sci. Eng. 112 (1992) 185.
[26] E.W. Larsen, The inverse source problem in radiative transfer, J. Quant. Spectrosc. Radiat. Transfer 15 (1975) 1.
[27] H.C. Yi, R. Sanchez, N.J. McCormick, Bioluminescence estimation from ocean in situ irradiances, Appl. Opt. 31 (1992) 822.
[28] C.E. Siewert, An inverse source problem in radiative transfer, J. Quant. Spectrosc. Radiat. Transfer 50 (1993) 603.

[29] C.E. Siewert, A radiative-transfer inverse-source problem for a sphere, J. Quant. Spectrosc. Radiat. Transfer 52 (1994) 157.

[30] N.J. McCormick, Unified approach to analytical solutions of three inverse transport problems, Prog. Nucl. Energy 34 (1999) 425.

[31] H.Y. Li, M.N. Ozisik, Estimation of the radiation source term with a conjugate-gradient method of inverse analysis, J. Quant. Spectrosc. Radiat. Transfer 48 (1992) 237.

[32] Z. Tao, N.J. McCormick, R. Sanchez, Ocean source and optical property estimation from explicit and implicit algorithms, Appl. Opt. 33 (1994) 3265.

[33] S. Stephany, H.F. de Campos Velho, F.M. Ramos, C.D. Mobley, Identification of inherent optical properties and bioluminescence source term in a hydrologic optics problem, J. Quant. Spectrosc. Radiat. Transfer 67 (2000) 113.

[34] H.Y. Li, A two-dimensional cylindrical inverse source problem in radiative transfer, J. Quant. Spectrosc. Radiat. Transfer 69 (2001) 403.

[35] H.M. Park, D.H. Yoo, A multidimensional inverse radiation problem of estimating the strength of a heat source in participating media, Int. J. Heat Mass Transfer 44 (2001) 2949.

[36] J. Su, A.J. Silva Neto, Two-dimensional inverse heat conduction problem of source strength estimation in cylindrical rods, Appl. Math. Modeling 25 (2001) 861.

[37] D.Y. Paithankar, A.U. Chen, B.W. Pogue, M.S. Patterson, E.M. Sevick-Muraca, Imaging of fluorescent yield and lifetime from multiply scattered light reemitted from random media, Appl. Opt. 36 (1997) 2260.

[38] J. Chang, H.L. Graber, R.L. Barbour, Imaging of fluorescence in highly scattering media, IEEE Trans. Biomed. Eng. 44 (1997) 810.

[39] H. Jiang, Frequency-domain fluorescent diffusion tomography: a finite-element-based algorithm and simulations, Appl. Opt. 37 (1998) 5337.

[40] J. Chang, H.L. Graber, R.L. Barbour, Luminescence optical tomography of dense scattering media, J. Opt. Soc. Am. A 14 (1997) 288.

[41] R. Roy, E.M. Sevick-Muraca, A numerical study of gradient-based nonlinear optimization methods for contrast enhanced optical tomography, Opt. Exp. 9 (2001) 49.

[42] J. Lee, E.M. Sevick-Muraca, Fluorescence-enhanced absorption imaging using frequency-domain photon migration: tolerance to measurement error, J. Biomed. Opt. 6 (2001) 58.

[43] M.A. O'Leary, D.A. Boas, X.D. Li, B. Chance, A.G. Yodh, Fluorescence lifetime imaging in turbid media, Opt. Lett. 21 (1996) 158.

[44] V. Ntziachristos, R. Weissleder, Experimental three-dimensional fluorescence reconstruction of diffuse media by use of a normalized Born approximation, Opt. Lett. 26 (2001) 893.

[45] J. Lee, E.M. Sevick-Muraca, Three-dimensional fluorescence enhanced optical tomography using referenced frequency-domain photon migration measurements at emission and excitation wavelengths, J. Opt. Soc. Am. A 19 (2002) 759.

[46] M.J. Eppstein, D.J. Hawrysz, A. Godavarty, E.M. SevickMuraca, Three-dimensional, Bayesian image reconstruction from sparse and noisy data sets: near-infrared fluorescence tomography, PNAS 99 (2002) 9619.

[47] V. Ntziachristos, R. Weissleder, Charge-coupled-device based scanner for tomography of fluorescent near-infrared probes in turbid media, Med. Phys. 29 (2002) 803.

[48] A.B. Milstein, S. Oh, K.J. Webb, C.A. Bouman, Q. Zhang, D.A. Boas, R.P. Millane, Fluorescence optical diffusion tomography, Appl. Opt. 42 (2003) 3081.

[49] A.D. Kim, A. Ishimaru, Optical diffusion of continuous-wave, pulsed, and density waves in scattering media and comparisons with radiative transfer, Appl. Opt. 37 (1998) 5313.

[50] R. Aronson, N. Corngold, Photon diffusion coefficient in an absorbing medium, J. Opt. Soc. Am. A 16 (1999) 1066.

[51] B. Chen, K. Stamnes, J.J. Stamnes, Validity of the diffusion approximation in bio-optical imaging, Appl. Opt. 40 (2001) 6356.

[52] R. Elaloufi, R. Carminati, J.-J. Greffet, Time-dependent transport through scattering media: from radiative transfer to diffusion, J. Opt. A 4 (2002) S103.

[53] A.H. Hielscher, A.D. Klose, K.M. Hanson, Gradient-based iterative image reconstruction scheme for time-resolved optical tomography, IEEE Trans. Med. Imaging 18 (1999) 262.

[54] A.D. Klose, A.H. Hielscher, Iterative reconstruction scheme for optical tomography based on the equation of radiative transfer, Med. Phys. 26 (1999) 1698.

[55] A.D. Klose, A.H. Hielscher, Optical tomography using the time-independent equation of radiative transfer. Part II: Inverse model, J. Quant. Spectrosc. Radiat. Transfer 72 (2002) 715.

[56] A.D. Klose, A.H. Hielscher, Quasi-Newton methods in optical tomographic image reconstruction, Inverse Problems 19 (2003) 387.

[57] A.D. Klose, A.H. Hielscher, Fluorescence tomography with simulated data based on the equation of radiative transfer, Opt. Lett. 28 (2003) 1019.

[58] R.A.J. Groenhuis, H.A. Ferwerda, J.J. Ten Bosch, Scattering and absorption of turbid materials determined from reflection measurements. 1: Theory, Appl. Opt. 22 (1983) 2456.

[59] W.F. Cheong, S.A. Prahl, A.J. Welch, A review of the optical properties of biological tissues, IEEE J. Quantum Electron. 26 (1990) 2166.

[60] S.A. Prahl, M.J.C. van Gemert, A.J. Welch, Determining the optical properties of turbid media by using the adding-doubling method, Appl. Opt. 32 (1993) 559.

[61] M. Born, E. Wolf, Principles of Optics, Cambridge University Press, Cambridge, MA, 1999.

[62] J.J. Duderstadt, W.R. Martin, Transport Theory, Wiley, New York, 1979.

[63] S. Chandrasekhar, Radiative Transfer, Oxford University Press, London, 1960.

[64] K.M. Case, P.F. Zweifel, Linear Transport Theory, Addison-Wesley, Massachusetts, 1967.

[65] E.E. Lewis, W.F. Miller, Computational Methods of Neutron Transport, Wiley, New York, 1984.

[66] B.G. Carlson, K.D. Lathrop, Transport theory – the method of discrete ordinates, in: H. Greenspan et al. (Eds.), Computing Methods in Reactor Physics, Gordon and Breach, New York, 1968, pp. 166–266.

[67] R. Sanchez, N.J. McCormick, A review of neutron transport approximations, Nucl. Sci. Eng. 80 (1982) 481.

[68] M.L. Adams, E.W. Larsen, Fast iterative methods for discrete-ordinates particle transport calculations, Prog. Nucl. Energy 40 (2002) 3.

[69] S.T Thynell, Discrete-ordinates method in radiative heat transfer, Int. J. Eng. Sci. 36 (1998) 1651.

[70] M.A. Ramankutty, A.L. Crosbie, Modified discrete ordinates solution of radiative transfer in two-dimensional rectangular enclosures, J. Quant. Spectrosc. Radiat. Transfer 57 (1997) 107.

[71] R. Koch, W. Krebs, S. Wittig, R. Viskanta, Discrete ordinates quadrature schemes for multidimensional radiative transfer, J. Quant. Spectrosc. Radiat. Transfer 53 (1995) 353.

[72] P.N. Brown, B. Chang, U.R. Hanebutte, Spherical harmonic solutions of the boltzmann transport equation via discrete ordinates, Prog. Nucl. Energy 39 (2001) 263.

[73] L.G. Stenholm, H. Stoerzer, R. Wehrse, An efficient method for the solution of 3-D radiative transfer problems, J. Quant. Spectrosc. Radiat. Transfer 45 (1991) 47.

[74] S.J. Wilson, T.S. Tan, Radiative transfer in a two-dimensional rectangular annulus medium, Math. Comput. Modeling 24 (1996) 29.

[75] A.D. Klose, A.H. Hielscher, Modeling photon propagation in anisotropically scattering media with the equation of radiative transfer, in: B. Chance, R.R. Alfano, B.J. Tromberg, M. Tamura, E.M. Sevick-Muraca (Eds.), Optical Tomography and Spectroscopy of Tissue V, Proc. 4955, SPIE, The International Society for Optical Engineering, Bellingham, WA, 2003, pp. 624–633.

[76] W.J. Wiscombe, The Delta-M method: rapid yet accurate radiative flux calculations for strongly asymmetric phase functions, J. Atmos. Sci. 34 (1977) 1408.

[77] A.J. Welch, M.J.C. van Gemert, Optical-Thermal Response of Laser-Irradiated Tissue, Plenum Press, London, 1995.

[78] S.R. Arridge, Optical tomography in medical imaging, Inverse Problems 15 (1999) R41.

[79] S.G. Nash, Linear and Nonlinear Programming, McGraw-Hill, New York, 1996.

[80] J. Nocedal, S.J. Wright, Numerical Optimization, Springer, New York, 1999.

[81] D.G. Luenberger, Linear and Nonlinear Programming, Addison-Wesley, Reading, MA, 1984.

[82] Ch.M. Bishop, Neural Networks for Pattern Recognition, Clarendon Press, Oxford, 1997.

[83] G.I. Marchuk, Adjoint Equations and Analysis of Complex Systems, Kluwer Academic Publishers, Dordrecht, 1995.

[84] M.E. Errico, What is an adjoint model?, Bull. Am. Meteorol. Soc. 78 (1997) 2577.

[85] R.E. Wengert, A simple automatic derivative evaluation program, Commun. ACM 7 (1964) 463.

[86] L.B. Rall, Automatic Differentiation: Techniques and ApplicationsLecture Notes in Computer Science 120, Springer, Berlin, 1981.

[87] L.B. Rall, G.F. Corliss, An introduction to automatic differentiation, in: A. Griewank, G.F. Corliss (Eds.), Automatic Differentiation of Algorithms: Theory, Implementation, and Application, SIAM, Philadelphia, 1991, pp. 1–18.

[88] O. Talagrand, The use of adjoint equations in numerical modeling of atmospheric circulation, in: A. Griewank, G.F. Corliss (Eds.), Automatic Differentiation of Algorithms: Theory, Implementations, and Application, SIAM, Philadelphia, 1991, pp. 169–180.

[89] T. Beck, Automatic differentiation of iterative processes, J. Comput. Appl. Math. 50 (1994) 109.

[90] R. Giering, T. Kaminski, Recipes of adjoint code construction, ACM Trans. Math. Software 24 (1998) 437.

[91] K.M. Hanson, G.S. Cunningham, S.S. Saquib, Inversion based on computational simulations, in: G.J. Erickson, J.T. Rychert, C.R. Smith (Eds.), Maximum Entropy and Bayesian Methods, Kluwer Academic Publishers, Dordrecht, 1998, pp. 121–135.

[92] T. Kaminski, M. Heimann, R. Giering, A coarse grid three-dimensional global inverse model of atmospheric transport. 1. Adjoint model and Jacobian matrix, J. Geophys. Res. 104 (1999) 18535.

[93] S.J. Norton, Iterative inverse scattering algorithms: methods of computing Frechet derivatives, J. Acoust. Soc. Am. 106 (1999) 2653.

[94] T.F. Coleman, F. Santosa, A. Verma, Efficient calculation of Jacobian and adjoint vector products in the wave propagational inverse problem using automatic differentiation, J. Comput. Phys. 157 (2000) 234.

[95] E.A. Ustinov, Adjoint sensitivity analysis of radiative transfer equation: temperature and gas mixing ratio weighting functions for remote sensing of scattering atmospheres in thermal IR, J. Quantum Spectrosc. Radiat. Transfer 68 (2001) 195.

[96] I.N. Polonsky, M.A. Box, A.B. Davis, Radiative transfer through inhomogeneous turbid media: implementation of the adjoint perturbation approach at the first order, J. Quant. Spectrosc. Transfer 78 (2003) 85.

[97] E.E. Graves, J. Ripoll, R. Weissleder, V. Ntziachristos, Sub-millimeter resolution molecular imaging system for small animal imaging, Med. Phys. 30 (2003) 901.

[98] R. Roy, A. Godavarty, E.M. SevickMuraca, Fluorescence-enhanced optical tomography using referenced measurements of heterogeneous media, IEEE Trans. Med. Imaging 22 (2003) 824.

[99] A. Godavarty, M.J. Eppstein, C. Zhang, S. Theru, A.B. Thompson, M. Gurfinkel, E.M. Sevick-Muraca, Fluorescence-enhanced optical imaging in large tissue volumes using a gain-modulated ICCD camera, Phys. Med. Biol. 48 (2003) 1701.

[100] J.C. Chai, H.S. Lee, S.V. Patankar, Ray effect and false scattering in the discrete ordinates method, Numer. Heat Transfer B 24 (1993) 373.

[101] A.H. Hielscher, R.E. Alcouffe, R.L. Barbour, Comparison of finite-difference transport and diffusion calculations for photon migration in homogeneous and heterogeneous tissues, Phys. Med. Biol. 43 (1998) 1285.